Alignment and integration of the first PLATO camera

P. Royer, A. Baeke, G. Terrasa, R. Huygen, S. Regibo, et al.

P. Royer, A. Baeke, G. Terrasa, R. Huygen, S. Regibo, J. Farinato, D. Magrin, A. Mazzoli, M. Pajas, B. Vandenbussche, A. Hermans, G. Millou, D. Vassallo, A. Belén Balado Margeli, L. Clermont, A. Cottinelli, L. Ferrari, N. Gorius, W. Laauwen, Y. Levillain, A. Novi, I. Pagano, M. Pertenais, G. Ramos Zapata, M. Salatti, T. A. Van Kempen, "Alignment and integration of the first PLATO camera," Proc. SPIE 12180, Space Telescopes and Instrumentation 2022: Optical, Infrared, and Millimeter Wave, 121804H (27 August 2022); doi: 10.1117/12.2628898

SPIE.

Event: SPIE Astronomical Telescopes + Instrumentation, 2022, Montréal, Québec, Canada

Alignment and Integration of the first PLATO Camera

P. Royer[a], A. Baeke[b], G. Terrasa[b], R. Huygen[a], S. Regibo[a], J. Farinato[c], D. Magrin[c], A. Mazzoli[b], M. Pajas[h], B. Vandenbussche[a], A. Hermans[b], G. Millou[b], D. Vassallo[c], A. Belén Balado Margeli[h], L. Clermont[b], A. Cottinelli[c], L. Ferrari[m], N. Gorius[f], W. Laauwen[m], Y. Levillain[k], A. Novi[g], I. Pagano[f], M. Pertenais[d], G. Ramos Zapata[h], M. Salatti[n], and T. A. Van Kempen[e]

[a]Institute of Astronomy, KU Leuven, Celestijnenlaan 200D bus 2401, 3001 Leuven, Belgium
[b]Centre Spatial de Liège, STAR Institute, Avenue du Pré-Aily, 4031 Angleur , Belgium
[c]INAF, Osservatorio Astronomico di Padova, Vicolo Osservatorio 5, 35122 Padova, Italy
[d]German Aerospace Center (DLR), Institute of Optical Sensor Systems, Rutherfordstr. 2, 12489 Berlin, Germany
[e]SRON Netherlands Institute for Space Research, Niels Bohrweg 4, 2333 CA, Leiden, The Netherlands
[f]INAF, Osservatorio Astrofisico di Catania, Via Santa Sofia 78, 95123 Catania, Italy
[g]LEONARDO SpA, via delle Officine Galileo 1, Campi Bisenzio, Florence Italy
[h]INTA, Carretera de Ajalvir, Km 4, 28850 Torrejón de Ardoz, Spain
[k]ESA-ESTEC, Postbus 299, 2200 AG Noordwijk, The Netherlands
[m]SRON Netherlands Institute for Space Research, Kapteynborg, Landleven 12, 9747 AD Groningen, The Netherlands
[n]ASI – Agenzia Spaziale Italiana, via del Politecnico, snc, 00133 Roma, Italy

ABSTRACT

PLATO is an exoplanet hunting mission of the European Space Agency. It is a medium-class mission, with a launch foreseen in 2026. Its prime objective is to uncover Earth-sized planets residing in their habitable zone.

The payload consists in 26 cameras with a very wide field of view. These cameras consist in a Telescope Optical Unit, aligned at ambient and characterised at the operational temperature, and a Focal Plane Array bearing the detectors, and delivered after coupling with the Front End Electronics.

In this contribution, we report on the alignment of the Engineering Model camera of Plato, i.e., the input metrology, the mechanical alignment of the optical unit with the focal plane array, the test environment and the optical characterisation throughout the process until the integrity check after delivery to the cryo-vacuum testing facility where the camera underwent a thorough performance demonstration. We also give a detailed description of the bolting process and the associated error budget.

Keywords: PLATO, AIT, AIV, camera, focus, alignment, bolting, integration, spacecraft integration

1. INTRODUCTION

The exoplanet hunting mission PLATO was selected as ESA-M3 candidate in 2014 in the framework of the Cosmic Vision Program. The prime mission objective is the hunt for exoplanets via the transit method[1,2] and the characterization of the host system, i.e. not only the radius, mass and density of the planet, but also the age of the system, by studying the host star with asteroseismology.[3–5] PLATO aims at discovering and characterizing exoplanets down to terrestrial-size planets, i.e. Earth-analogues residing in the habitable zone around their host star. A complete description of the science objectives can be found in Ref. 6.

Further author information: (Send correspondence to P. Royer)
P.Royer: E-mail: pierre.royer@kuleuven.be

Space Telescopes and Instrumentation 2022: Optical, Infrared, and Millimeter Wave, edited by Laura E. Coyle, Shuji Matsuura, Marshall D. Perrin, Proc. of SPIE Vol. 12180, 121804H · © 2022 SPIE · 0277-786X · doi: 10.1117/12.2628898

The mission was adopted in 2017[7] and entered in implementation phase thereafter. The Engineering Model camera was successfully integrated and validated under cryo-vacuum at the end of 2021, allowing the mission to pass ESA's Critical Milestone earlier this year, confirming the mission is on track for launch in 2026.

The PLATO spacecraft consists in 26 cameras, all sharing the same optical design. They are refractive telescopes, with an optical train made of 6 lenses, as described in 8, 9 and references therein. Each camera consists of three main components. The Telescope Optical Unit (TOU) bears the optical elements;[9] the Focal Plane Array[10 11] (FPA) bears the four 4510×4510 pixels CCD detectors and the Front End Electronics (FEE) contains the readout electronics.[12] The payload is composed of 4 groups of 6 cameras pointing at the same portion of the sky. All groups are pointing in different directions, 9.2 degrees away from the two remaining cameras, the so-called Fast Cameras, operated at a cadence of 2.5 sec (vs 25 sec for the others), and used as Fine Guiding System.

The Assembly, Integration and Verification of the cameras and payload is described in 13 and 14. In a nutshell, the TOU tube is fabricated by the University of Bern (Switzerland). The lenses are installed and aligned by Leonardo (Florence, Italy; hereafter LDO). On the other side, the FPA structure is produced by LIDAX, for INTA (Spain). The CCDs are tested by MSSL (UK) and shipped to Spain for integration and alignment with the structure. The FPA is then sent back to the MSSL, where it is mated with the FEEs (also produced there) and finally delivered to CSL (Belgium). CSL assembles the TOU with the FPA and delivers the camera to a Test House for thermal cycling and a full characterization of the camera performance under cryo-vacuum conditions. While the flight model cameras will each be sent to a single test house, the Engineering Model (EM) will be sent to all three test houses, being SRON (Netherlands), IAS (France) and INTA (in this order), in order to validate the GSEs, test plans and AIV processes at all premises.

The present paper discusses the operations performed in CSL with respect to the alignment and assembly of the TOU and FPA+FEE into a camera. The prime objective is to couple the FPA with the TOU, i.e. to position the sensitive plane of the FPA (the mid-plane formed by the four detectors) at the exact same location as where the Best Image Plane (BIP) produced by the TOU will exist in operational conditions. As explained in Ref. 15, two methods were originally envisaged for the camera alignment:

- an 'optical' method, in which the location of the BIP is measured with respect to a reference plane. The reference plane would be obtained from optical measurements performed at ambient temperature and independently by the TOU and the alignment teams. That is hence an indirect method which requires a high accuracy determination of the location of both the BIP at cold and the reference plane at ambient by the TOU team. It does on the contrary not require any advanced metrology on the sensitive plane of the FPA (hereafter FPA_SEN).
- a 'mechanical' approach in which the location of the BIP is directly given with respect to the mechanical reference frame attached to the TOU (hereafter TOU_MEC). This method imposes an accurate determination of the position of the mean sensitive plane of the detectors with respect to a mechanical reference frame attached to the FPA.

Scheduling constraints combined with the possibility to derive the appropriate metrology on the FPA finally advocated for the adoption of a hybrid solution. The mechanical approach is kept as baseline, but an optical verification is performed at ambient, with two goals in mind: **a.** secure the consistency between the TOU metrology obtained at Leonardo at TOU level and at CSL at proto-camera level, and **b.** verify the consistency between the measurements performed by LDO with a service detector (esp. the BIP; see Ref 16) and those obtained in CSL with the actual camera detectors.

The next section presents the test environment and Ground Support Equipments (GSEs). Sections 3 and 4 present the alignment principles and the results from the optical verifications performed in the process. Finally, section 5 describes the bolting process, and the optical verification of the system stability until the end of the cryo-vacuum campaign at SRON.

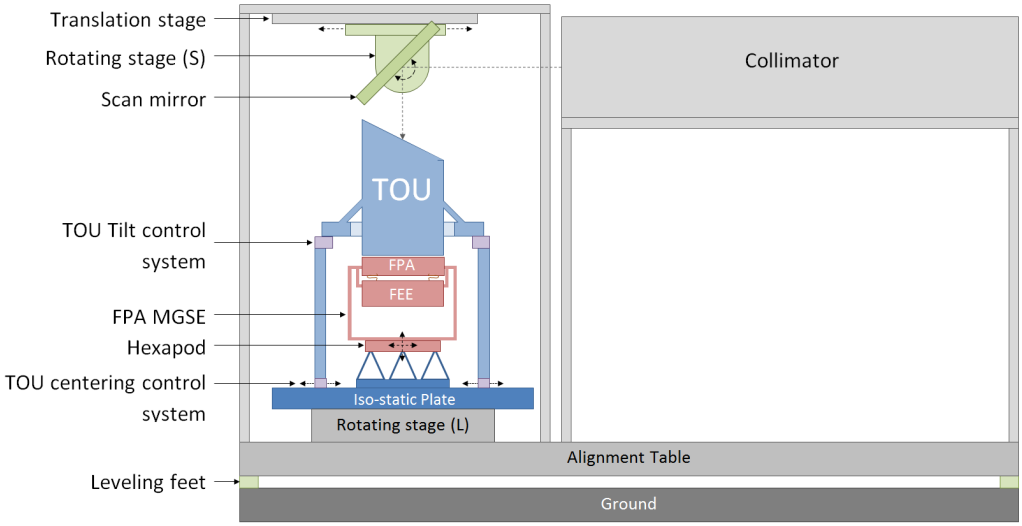

Figure 1. Alignment setup layout. The scan mirror assembly (translation and rotation stage 'S') allows to modify the elevation angle under which the collimated beam is sent to the camera. The big rotation stage supporting the camera allows to modify the azimuth.

2. TEST ENVIRONMENT

2.1 Mechanical and Optical Ground Support Equipment

The alignment and camera integration take place in an ISO 5 cleanroom. An electronic rack gathers the electronics (section 2.2). The Optical Ground Support Equipment (OGSE) consists in a Laser Driven Light Source (also located in the electronic rack), feeding a collimator via an optical fiber, after passing through two filter wheels allowing to control the light intensity via neutral density filters.[17]

The rest of the setup is presented in Figure 1: the camera is mounted vertically, and the light from the OGSE is deflected towards it via a flat mirror (here after "the scan mirror").

The necessity to explore any part of the camera field of view is met by three mechanisms:

- a small rotation stage supports the flat mirror, and allows for modifications of the elevation angle used to illuminate the camera (θ; angle from the optical axis)
- a translation stage supports the small rotation stage and the flat mirror, and allows to preserve a full-pupil illumination regardless of the selected elevation.
- a large rotation stage supports the entire camera, and allows for modifications of the azimuth (ϕ).

An isostatic plate is mounted on the big rotation stage. The TOU is mounted on it, and it is fixed with respect to it. The FPA also stands on the isostatic plate, but it is supported by a hexapod to allow for its free placement with respect to the TOU. The system hence gathers nine degrees of freedom: six linked to the hexapod and three to the three translation and rotation stages.

The large rotation stage rotation axis defines the main reference frame of the setup while the position and orientation of the main reference frame is materialized by laser tracker targets and measured with a laser tracker. The scan mirror and the collimator are also equipped with laser tracker targets used to define the reference frames of both items and therefore also the position of their optical centre and the orientation of their optical axis. The collimator is aligned perpendicular and the mirror is aligned at 45° with respect to the main reference frame using the laser tracker. The alignment is performed with an accuracy of 15 arcsec in orientation and 60 μm in position. The alignment result is calibrated with an accuracy of 8 arcsec in orientation and 15 μm in position.

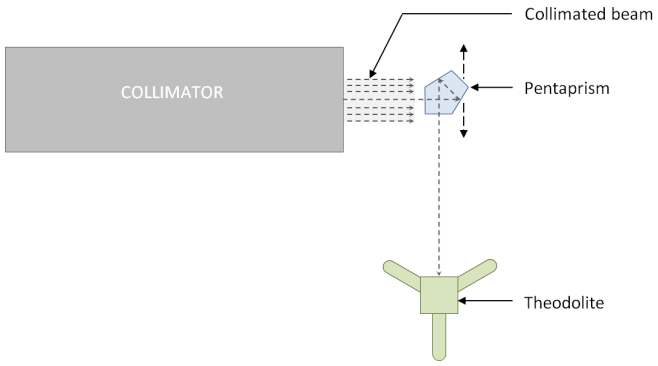

Figure 2. Theodolite and pentaprism layout during OGSE calibration error verification.

This way, the orientation of the field of view angle (θ, ϕ) that is sent towards the TOU is known with an accuracy of 8 arcsec.

The collimation error of the OGSE (collimator and scan mirror) is verified within CSL facilities using a pentaprism and a theodolite (see Figure 2). The pentaprism is set at one edge of the exit beam of the collimator and the crosshair of the theodolite is co-aligned with the reflected beam to allow for the horizontal angle to be registered. The pentaprism is moved towards the other edge of the collimator beam and the movement of the horizontal angle is followed during this movement. During verification performed on the setup, no visible movement of the horizontal angle has been observed meaning that the collimation error is negligible.

2.2 Electrical Ground Support Equipment

2.2.1 Pointing

The collimated beam of the OGSE simulates a single point source at infinity. The combined movements of the three stages allow to point it at any $[\theta, \phi]$ position in the field of view. The movement of the translation stage is limited to one side of the optical axis ($\theta \geq 0$). To avoid any issue with the cables connected to the FEE through the hexapod, the movement of the big rotation stage is limited to 360 degrees ($\phi \in [-180, 180]$). The translation and rotation of the scan mirror are driven by the desired target elevation and can be written

$$\Delta x = h \cdot \tan\theta \tag{1}$$

$$\alpha = \theta/2 + k_1 \cdot \theta + k_2 \cdot \theta^2 \tag{2}$$

respectively, where Δx describes the translation stage position, h is the height of the translation stage above the entrance pupil of the camera and α is the inclination of the scan mirror with respect to the vertical direction. The first term in equation 2 is purely geometrical. The correction terms are necessary because the SMA translation stage is not perfectly rigid, but presents a small bending along its travel path. The coefficients (k_1, k_2) were determined via theodolite measurements giving the actual rotation angle of the mirror as a function of the commanded one. The correction is expressed in θ rather than Δx. Given the monotonic relation between them reported in equation 1, it is equivalent.

The azimutal angle ϕ is fully characterised by the orientation of the big rotation stage, as depicted in Fig. 3. A correction is nevertheless necessary due to a small misalignment of the SMA in rotation around the vertical direction, inducing an elevation-dependent error in azimuth, increasing towards the optical axis. This can be accounted for by adapting the command to the big rotation stage:

$$\phi_{commanded} = -\phi_{target} + \Delta\phi(\theta) \tag{3}$$

where the minus sign expresses the necessity to rotate the setup in the opposite direction with respect to the desired azimuth, and $\Delta\phi(\theta)$ is drawn from a correction table derived from a geometrical model of the setup. This correction was not used for the EM camera. For the flight models, the correction will be activated. Given the rotational symmetry of the optics, the effect of this misalignment on the alignment is negligible.

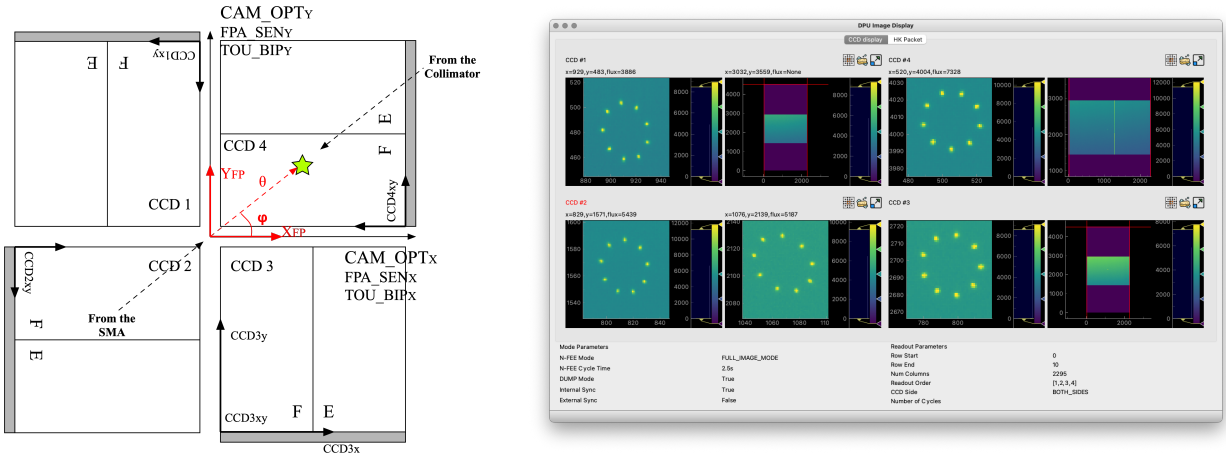

Figure 3. **Left:** Focal-plane reference frame (x_{FP}, y_{FP}), with the definition of the field angles θ (elevation) and ϕ (azimuth) used for commanding the MGSE. The four CCDs have their own coordinate systems for the data acquisition. The location of the readout registers is displayed in gray. It is the goal of the alignment to make the reference frames attached to the best image plane (TOU_BIP) and the mean sensitive plane of the detectors (FPA_SEN) coincide. CAM_OPT represents the resulting reference frame (section 3). **Right:** The data processing unit GUI, displaying the four detectors. Each CCD has 2 readout amplifiers, hence 2 independent images. The images in some of the panels were zoomed in to inspect the Hartmann pattern (section 4. In the others, the effect of the partial readout is visible, as only a subset of the detector is readout. The telemetry at the bottom of the display report on the current operational mode of the FEE.

2.2.2 Operational Environment

The Electrical Ground Support Equipment (EGSE) and the commanding of the instrumentation is written in Python. All details about the infrastructure can be found in Ref.[18] The camera tests are commanded from a standard Python IDE, by executing so-called 'building blocks'. A building block is a Python function fitted with a specific decorator. The roles of the decorator are to **a.** make sure only certified scripts are executed on the operational machine, **b.** verify that all parameters are properly specified, **c.** make sure that the building blocks are always executed within an observational context and therefore associated with a unique observation identifier (obsid).

During the test execution, the operator can follow the progress in real time via a collection of GUIs tracking the status of the entire setup: all egse processes, the image acquisition system, including real-time telemetry and image displays, the mechanisms, the positions in the field of view that were visited since the start of the observation, etc (Figure 3). In addition, the housekeeping is processed with Prometheus and can be visualised in a simple web browser via an extensive collection of Grafana dashboards covering all sub-systems (MGSE, OGSE, FEEs, detectors, test chamber, thermal control, ...).

The telemetry and image data produced during a test campaign are stored in a different directory every day. In addition, when an observation starts, a dedicated directory is created where the data produced during the corresponding time window is duplicated. This allows for an easy analysis of the data both on the long-term (e.g. thermal) and short term, i.e an easy selection of the data relevant for each observation.

The telemetry from the camera and from the facility are stored in csv files. The raw stream of image data is stored in HDF5 files, which are then assembled into data cubes in FITS format for the sake of convenience. The FITS file generation is automatically triggered either by the end of an image acquisition command, or by a specific commanding parameter allowing to split the very large data cubes in smaller, manageable slices.

In the most demanding observing modes, almost 400 MB are generated every minute. The data are transferred to a fast SSD drive in real time, and duplicated to a larger storage in near real time. Finally, the data archive is duplicated to an FTP server on the KU Leuven premises, via a rsync command running every 15 minutes. That way, the data from the alignment and integration of all PLATO cameras obtained at CSL, and the data from the test campaigns at the three test houses (Section 1) is made available to the consortium in one central location.

3. MECHANICAL ALIGNMENT

The process of camera alignment and integration can be decomposed in a few steps:

1. **Installation**. Position the FPA and the TOU on the test setup
2. **Approach**. Approach the FPA from the TOU so that FPA_SEN coincides with the RF attached to the BIP (hereafter TOU_BIP).
3. **Verification**. Perform an optical verification of the metrology, i.e. check the consistency between the measures performed at TOU and camera levels
4. **Correction**. Apply the corrections necessary to account for the differences between the ambient and the flight conditions.
5. **Integration**. Bolt the FPA onto the TOU

The goals of step 1 are a. on the FPA side, to locate the reference frame with respect to which FPA_SEN is known (hereafter FPA_ALN); b. on the TOU side, to locate the reference frame with respect to which the position of the BIP is known (hereafter TOU_MEC); c. to position the TOU on the setup such that the optical axis of the camera coincides with the optical axis of the collimator of the OGSE and the rotation axis of the main rotation stage (section 2.1).

The mechanical reference frames TOU_MEC and FPA_ALN are defined by the coordinates of Laser Tracker Targets attached to the mechanical structures of the TOU and the FPA respectively. The alignment of the TOU with the optical axis of the OGSE is made via an optical cube attached to the TOU, whose orientation with respect to the optical axis is measured at TOU level.

All the metrology defining the reference frames TOU_ALN, TOU_MEC, TOU_BIP, FPA_ALN and FPA_SEN is produced at subsystem level and delivered to CSL with the hardware.

The location of the last optical surface is also characterized by the TOU team for the following reason: prior to the approach (step 2), an avoidance volume is defined around it to avoid the risk of collision between the detectors and the optics while manipulating the FPA. This is especially important since after positioning the FPA onto the BIP, the last lens comes as close as 1.5 mm from the nearest mechanical part and about 2 mm from the detectors' surface, while the straylight mask around the detectors prevents any direct visibility of the interstitial volume for the most critical part of the approach (last $\sim$1 cm).

After installing the TOU and the FPA on the setup and after homing the hexapod, a mathematical model of the entire mechanical setup is established. It includes close to twenty different reference frames and their relations. In addition, 60 verification points are defined 300 μm above the detector, at the edge of the FPA. Together they define a 'security volume' around the FPA. Throughout the alignment, the collision avoidance is then verified by software: the commands are not directly sent to the hexaopod but to the model. After the virtual movement, it is verified that none of the verification points has entered the avoidance volume. If the answer is negative, the movement is allowed and the command is transferred to the hexapod.

In order to maximize the effective field of view covered by all cameras of a given group, i.e in order to maximize the on-sky overlap between the fields of view of the individual cameras, it is important that the detectors are also aligned rotationally around the optical axis, between cameras. This is automatically taken care of during the approach by adjusting the position of the FPA to the reference frame that will be used later in the AIV to integrate the cameras on the spacecraft (hereafter CAM_BOR). To this aim, the TOU_BIP reference frame is defined such that its x-axis points to the reference axis of the camera (which can slightly differ from TOU_MEC), and the FPA_SEN reference frame is defined such that its x-axis is aligned with the rows of a reference detector. Forcing those to coincide for all cameras ensures we are using the same external reference for all cameras and hence cancels any potential rotational misalignment between their respective fields of view. This explains why CAM_BOR, TOU_BIP and FPA_SEN coincide in Figure 3.

At the end of the approach, but prior to the optical verification, we rotate the camera by 360 degrees and obtain 20 images evenly distributed in azimuth, all at a given elevation. The center of the circle fitted to the

coordinates of the sources provides an empirical estimate of the de-centering of the FPA with respect to the optical axis. No correction was applied at this point for the EM camera though. A good centering of the FPA was nevertheless confirmed by the cryo-vacuum measurements performed. The de-centering is fit along with the optical model and is found to be 6 - 10 pixels.[19] The optical verification is described in section 4.

Finally, the correction terms necessary at step 4 can be found in Ref. 15 (their equation 2). They include:

- the translation from FPA_SEN at ambient to the operational temperature. For the EM camera, this correction amounts to $75\,\mu m$. It corresponds to the thermal contraction of the support bipods of the FPA. For the EM camera, slight deformations of the FPA structure were observed at the operational temperature, which were also included in the correction. This problem has been solved for the flight model cameras, and this additional contribution should consequently not be necessary anymore.
- the translation from TOU_BIP resulting from the difference in thermal gradients along the camera during the measurements at TOU level (isothermal camera) with respect to the flight conditions, where the heat generated by the FEEs is dissipated radiatively by the baffle of the camera, hence imposing a temperature gradient in the direction of the optical axis. This correction amounts to $12\,\mu m$.
- the translation resulting from the compression of the shims and the mechanical embedding taking place in the days following the bolting of the FPA on the TOU (section 5). This correction amounts to $35\,\mu m$.

4. OPTICAL VERIFICATION

Once the focal plane is in place at the location of the BIP, but before bolting the FPA onto the TOU, a consistency check of the metrology is performed between the proto-camera (CSL) and the TOU (LDO). It also serves the purpose to verify the absence of effect due to the use of a service detector to determine the location of the BIP in LDO, while the alignment and cryo-vacuum performance verifications happen with the actual PLATO focal plane array of detectors. To this aim, a series of optical measurements are performed at ambient temperature with the detector at the location of BIP; first at TOU level, and later on reproduced during the camera alignment.

4.1 Acquisition principle

The nominal operational temperature of the PLATO cameras is $-80\,°C$. At ambient temperature, 100 degrees warmer, the size, shape, relative positions and refractive indices of the lenses are different, hence strongly degrading the optical performances. In addition, at ambient temperature, the best image is on average 1.5 mm further from the last optical surface than at the operational temperature, and there is a strong field curvature, of $\sim 500\,\mu m$ from the center to the edge of the field. In order to cope with the strong defocus, the measures are performed through a hartmann mask (identical at both premises) which was placed in the collimated beam of the OGSE. A full-aperture approach was considered originally,[20] but simulations have demonstrated that the data reduction would be simpler and that the results would be more accurate with the current approach. In order to account for the strong field curvature, the data analysis is split by elevation angle wherever relevant.

The strong dark current at ambient imposes short exposure times, which is impossible with PLATO's Auxiliary Electronic Units providing the clock and synchronization pulses triggering the detector readouts to the FEEs. Therefore, at ambient temperature, the synchronisation pulses are directly generated by the FEEs. In addition, to limit the duration of the readout, the dark current and the amplitude of the readout smearing (given there is no shutter in the path), the CCDs are operated in partial readout, i.e. only 1500 rows of one CCD are readout around the source. The location of the source on the focal plane is pre-computed, including a standard model of the optical distortion of the cameras. In addition, a complete CCD clearout is performed before every exposure, to minimise the impact of the dark current accumulated during the readout of one exposure onto the next one.

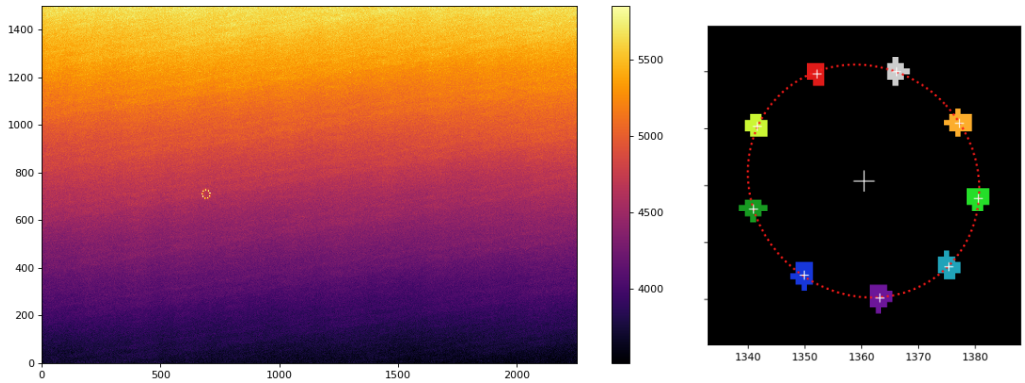

Figure 4. **Left**: raw image. The strong background variation is due to the high dark current at ambient temperature, accumulating during the frame readout, occuring bottom-up. **Right**: Final stage of the data reduction. After background subtraction, the pixels significantly above the noise are labelled; an ellipse is then fit to the centroids of the hartmann-spots.

4.1.1 Data reduction

Figure 4 shows an example image. The top panel of the figure shows the hartmann pattern on top of a strong, and strongly varying background, due to the dark current accumulating during the exposure and during the readout. The bottom panels present zooms on the hartmann pattern, in the raw image on the left, and in the reduced one on the right. The data reduction proceeds as follows:

Background subtraction: The background is computed by sequentially applying a median filter, to remove the sources and a gaussian filter, to smooth out the noise, both with wide kernels.

Thresholding: The pixels appearing significantly above the noise are stored in a binary mask. Yen's thresholding method was found to be the most efficient.[21]

Cleaning: Isolated pixels (cosmetic defects, cosmic rays impacts) are removed from the mask by binary opening. This step was introduced based on simulations, but thanks to the very short exposure times used in practice (< 1 sec), it could have been omitted.

Labelling: The 'islands' formed by the individual hartmann spots in the binary mask are identified and labelled individually. A centroid is then computed for every spot.

Fitting: An ellipse is fit through the spot-centroids, although the difference with fitting the ellipse to the binary mask directly is most of the time negligible.

To make sure that the differences between test premises weren't linked to the data reduction, the data produced at LDO were reduced in double-blind by two totally independent codes. The results were shown to vary by as much as 0.3 pixels on average, in terms of size of the ellipse. That corresponds to the error budget of the alignment, hence proving the paramount importance to reduce all data with the same algorithm before comparison. The steps in the procedure accounting for most of the differences were shown to be the background subtraction and the thresholding.

4.1.2 Analysis

The metric used to compare measurements and estimate the defocus, i.e. the relative movement along the optical axis (hereafter 'z') is the 'diagonal' size of the ellipse, i.e. $\Sigma \triangleq \sqrt{a^2 + b^2}$, where a and b refer to the semi-major and semi-minor axes of the ellipse respectively. That proved to be much more robust than either a or b in the presence of noise, especially when the two values are close to each other and can be inverted by the fitting routines.

We calibrated the sensitivity of Σ vs defocus via measures obtained by moving the FPA over $300\,\mu m$ along the optical axis close to the BIP. We found a value of

$$\tau \triangleq \frac{dz}{d\Sigma} = 65\ [\frac{\mu m}{pix}] \tag{4}$$

that is constant in the central part of the field but decreases towards the edges, with $60\,\mu m/pix$ at 12.4 degrees of elevation, and 50 at 16.33 degrees.

We estimated the sensitivity of the hartmann measurements by repeating the same series of measures performed at 20 positions in the field of view, equally spaced in azimuth, at an elevation of 8.3 degrees. The measures are repeated seven times, including two executions with a mini-dither of half a pixel in x and y directions to estimate the sensitivity with respect to the projection of the hartmann spots on the pixel grid. The results are shown in Figure 5 in gray (repetitions) and blue (dithers). The overall reproducibility is $\leq 1\,\mu m$ when comparing the groups of 20 measures, with a dispersion $\sigma \leq 3\,\mu m$ at any given value of the azimuth.

Assuming that the measurement differences are not dominated by systematic errors, the agreement between two sets of measurements A and B (e.g. CSL vs LDO or pre- vs post-bolting) can be verified by the following relations:

$$\delta\Sigma_{global} = |\frac{1}{N}\sum_{i=1}^{N}(\Sigma_{Ai} - \Sigma_{Bi})| < \delta\Sigma_{max} + 3 \cdot \frac{\sqrt{2} \cdot \sigma_\Sigma}{\sqrt{N}} \tag{5}$$

$$\delta\Sigma_{local} = \max_N |(\Sigma_A - \Sigma_B)| < \delta\Sigma_{max} + 3 \cdot \sqrt{2} \cdot \sigma_\Sigma \tag{6}$$

where N is the number of independent measurements (locations visited in the field of view), σ_Σ is the measurement uncertainty and $\delta\Sigma_{max} \sim 0.3$ pixel is the maximum difference allowed by the focus requirements (derived from the alignment error budget $dz_{max} = 20\,\mu m$ via equation 4). It dominates the second term in equations 5 and 6 since, as seen above, in absence of systematics $\sigma_\Sigma \lesssim 3\mu m \sim 0.05$ pixel. The first criterion ensures a global agreement over the entire dataset, given the measurement errors (H_0 hypothesis that the means of the two sets agree within $\delta\Sigma_{max}$); the second criterion verifies the absence of unacceptable local deviations in the field of view.

4.1.3 Results

Whereas the metrology of the LTTs on the FPA side provided a very accurate definition of the alignment reference frame of the FPA, it had not been determined with the same level of accuracy on the TOU side for the EM camera (LDO). It was nevertheless used to locate the TOU mechanical reference frame on the alignment setup (CSL). This misunderstanding about the interface led to a miscalculation in the z direction at proto-camera level, i.e. an error in the relative positioning of the FPA and TOU on the alignment setup. That was immediately detected thanks to the optical verification. The mechanical reference frame of the TOU was then remeasured by moving a laser tracker target over the interface plane defining it. A correction of $65\,\mu m$ was found and applied, restoring the agreement between the measurements at TOU and proto-camera level with respect to the defocus. To prevent similar issues for the flight model cameras, the metrology of the TOU_MEC reference frame will be transferred from TOU to camera level via the coordinates of the centers of reference spheres positioned in laser tracker nests, measured on both premises.

At TOU-level, the reference hartmann measurements were performed by moving a small detector inside a plane (hereafter the "Hartmann plane"). That plane should have been identical to the BIP, measured at cold temperature, but due to metrology issues at ambient for the EM camera, it was actually shifted by about $200\,\mu m$ in the focus direction, and tilted with respect to the optical axis. Consequently, at proto-camera level, while the agreement found in the focus direction was very good, a discrepancy in tilt appeared, inducing a sine-wave signature in the curve of Σ vs azimuth.

That signature is visible in Figure 5 and corresponds to tilts of 1.4 and 4 arcmin at TOU and proto-camera level respectively, in different directions. The corresponding systematic error dominates equations 5 and 6, which consequently prevented a formal validation of the metrology. Nevertheless, given the known issues with

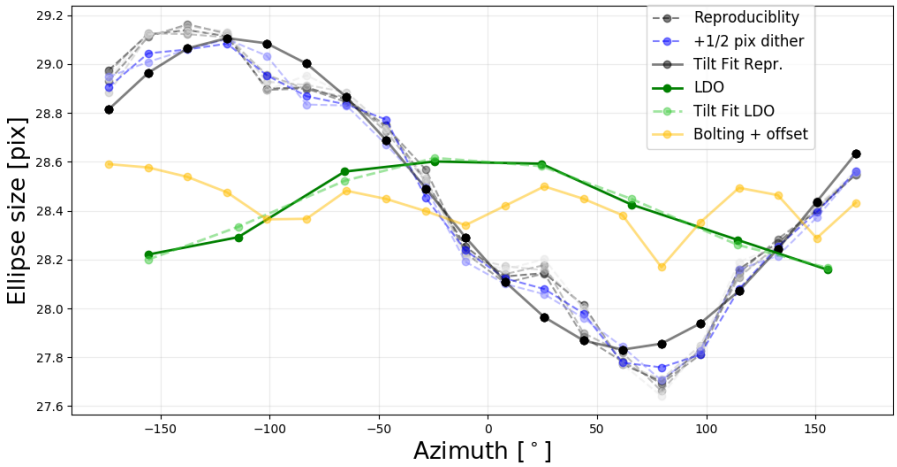

Figure 5. Optical verification measurements: size of the Hartmann pattern as a function of the azimuth, for a constant elevation of 8.3 degrees. Green: reference measurement at TOU-level. Gray and blue: measurements at proto-camera level, including assessment of reproducibility. Orange: comparison measurement performed at the location of the bolting plane (which is parallel to the BIP), including an offset of 300 μm for visualisation purposes. The black and lightgreen curves are sine-waves fitted to TOU and proto-camera level data points. The agreement in focus is good on average (y-axis), but the measurement planes are tilted with respect to each other (see text for details). The four 'waves' visible in the measurements performed at proto-camera level (orange) are likely explained by the non-flatness of the CCD detectors.

the definition of the Hartmann plane for this camera (corrected for the flight model[16,22]), given the agreement in the focus direction, and given that the Best Image Plane did not present any such tilt with respect to the optical axis (orange curve in Figure 5), the verification was accepted and the the FPA was aligned on the BIP, as planed. The metrology of the FPA, the TOU, the BIP and the camera alignment were later validated by the cryo-vacuum tests of the camera performed in SRON (NL). As reported in Refs 19,23, 13,14, the alignment budget in focus and tilt, and the general optical performance of the camera was indeed found fully compliant with the requirements.

5. CAMERA INTEGRATION

Once the correct location and orientation of the FPA sensitive area with respect to the TOU are defined, the two components can be bolted together. They are connected together at three different points located at the circumference of the FPA. The FPA bolting interfaces to the TOU is composed of 3 bipods and the TOU interfaces to the FPA are 3 interface planes. At the nominal position of the FPA with respect to the TOU, the gap between both interfaces is $\sim$7 mm. This gap is filled with spacers which thickness is estimated by measuring the distance between the interfaces after the mechanical alignment process and the alignment verification. The spacers are inserted between the two interfaces during the bolting process.

Performing the alignment and camera integration consistently on a series of 26 cameras within a tight schedule and with the required accuracy (20 μm) represents a significant challenge in terms of AIV flow. Small variations on the interfaces geometry can cause large discrepancies between the predicted thickness needed and the final spacer thickness to be used in practice. The gap measurement is performed to help reduce the number of iterations needed to find the correct set of spacers. During the EM alignment campaign, the bolting was performed in only two iterations, while 3 were anticipated. With further specimens, the end goal is to be able to perform it in only one.

The complete bolting process, can be decomposed as follows :

- The distance between the TOU and FPA bolting interfaces is measured to give a first estimate of the required spacer thickness (gap measurement).
- The spacers are selected accordingly, and installed (after lowering the FPA).
- The FPA is elevated until the spacers are pinched between the TOU and the FPA interface.
- The rest of the bolting stack and a tensioning tooling are installed.
- All three interfaces are loaded, at the same time.
- The interfaces are locked and the tension is released.
- The tensioning equipment is removed and a full optical verification is performed. The full optical verification is repeated the next day.

If successful, the bolting process is completed. If not, the process is repeated with a new set of spacers.

5.1 Gap measurement

The measurement is performed using a gauge block with a known and accurate thickness of 1.000 mm placed at the top side of the FPA bipod. A digital comparator is then mounted in the interface hole of the TOU and is set to zero before the start of the measurement.

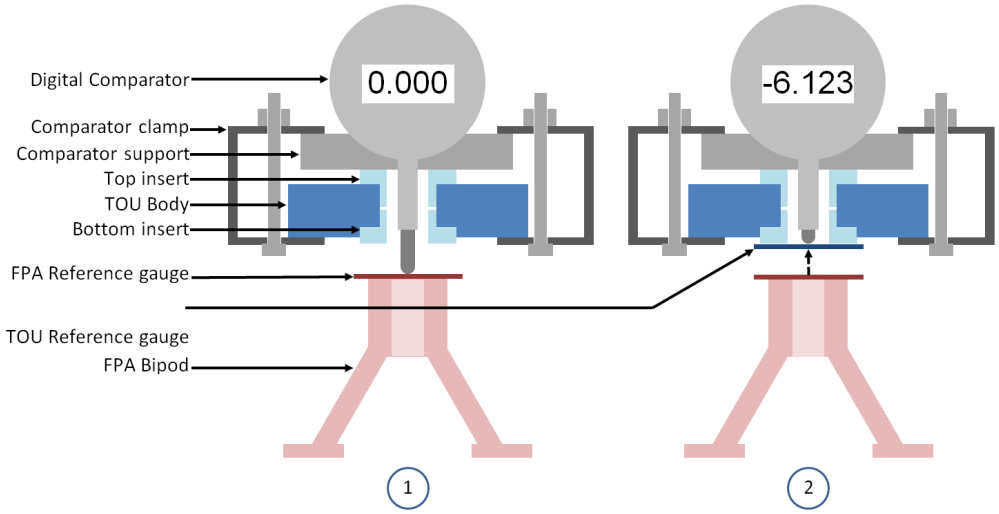

Figure 6. Gap measurement principle. 1. The comparator needle is in contact with the FPA reference gauge. 2. The needle is in contact with the TOU reference gauge to measure the gap.

A second gauge is placed in contact with the TOU bolting interface and the comparator value is registered. The comparator needle is then left to slowly return to its original position and the value is registered. The measurement process is repeated 10 times with two different operators (total of 20 gap measurements taken per interface) and the average value is taken. The spacers size is selected to be slightly larger than the measured value to account for the compression of the stack but also other possible error contributors such as the embedding of the mating surfaces.

In the mechanical assembly linking the hexapod to the FPA, compliant parts are used to limit the load on the FPA and the hexapod during the bolting process. These compliant parts are designed to be flexible in the vertical direction but stiff in the other directions. Since there is no contact between the FPA and the TOU during the alignment, the parts are not solicited and the FPA stays fixed relative to the hexapod. This is no longer the case during the bolting where the parts can deform vertically to accommodate the FPA movement toward the TOU during the bolting. Hence, once the gap measurement is performed, the comparators are removed from the TOU and installed to register the vertical displacement between the FPA and the hexapod.

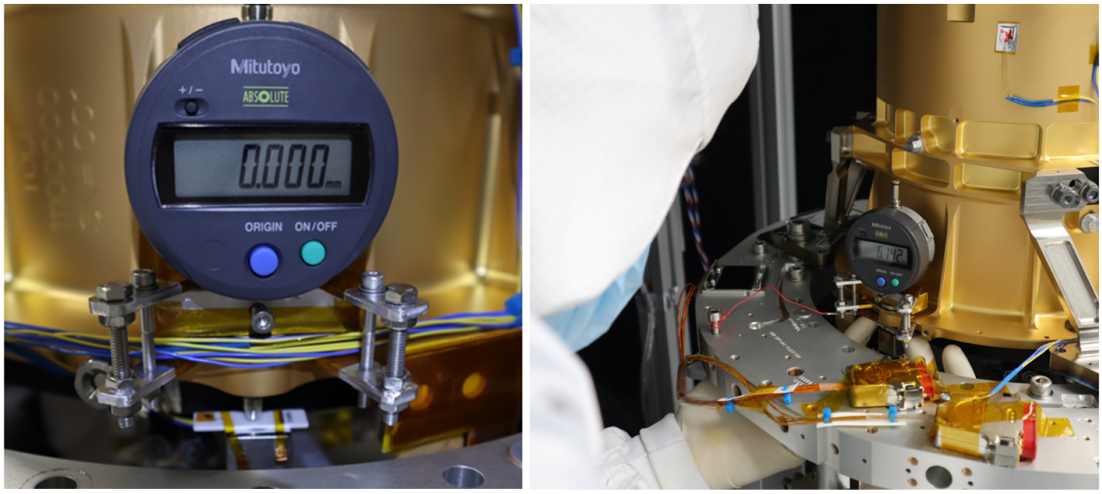

Figure 7. **Left:** Bottom reference gauge on the FPA bipod. Comparator installed and initialized on the bottom reference gauge. **Right:** Gap measurement performed by putting the top reference gauge in contact with the TOU bottom insert surface.

5.2 Bolting principle

During the bolting process, Hartman images are regularly taken at one fixed location in the field of view. For every image, the ellipse size and the related z-position are calculated. They are compared with those obtained from the first image, taken just after the optical verification and used as a reference.

After the alignment and gap measurement but prior to the bolting, the hexapod holding the FPA is moved to a lower position to allow for the installation of the spacers and the bolting studs. Once the spacers and the studs are installed, the hexapod is moved upward in small steps until the spacers resting on the FPA bipods are in contact with the TOU interface. Once the contact is effective, the rest of the bolting stack and the bolt tensioning tooling are installed. A hydraulic bolt tensioner is used for the bolting instead of a torque wrench to prevent rotation of the screw during torquing. An additional advantage of this method for tensioning the bolts is that the 3 bipods can be torqued at the same time.

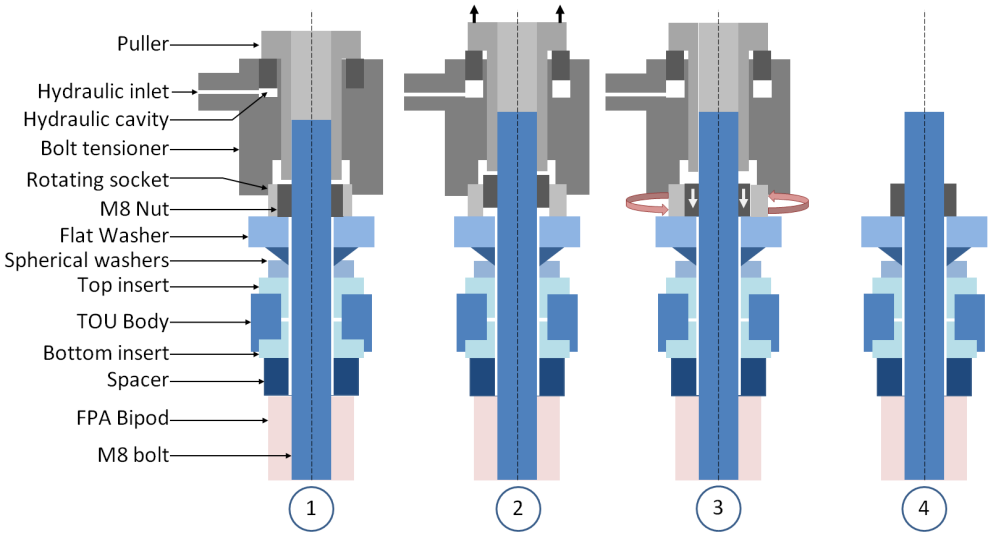

Figure 8. Bolt tensioner operating principle on FPA-TOU interface. See text for details.

By increasing the pressure in the hydraulic tensioner cavity (step 2 in Figure 8), the bolts are elongated until the desired elongation/load is reached. By turning the socket (step 3 in Figure 8), the nut is then locked to freeze the elongation at the desired level and the pressure in the tooling is released. To lock the nut, a 2 Nm torque is applied to ensure good repeatability of the process. Considering the bolts are loaded at approximately 24 kN at this point in the process, the small torque applied does no causes any relative movement between the TOU and the FPA. The pressure release causes a small decrease of the load in the bolt which requires the pressure prior to the bolting to be higher than the desired final pre-load. The overload was determined on the STM camera model, which had the same design as the Engineering and Flight Models. The load was measured using an echo-meter to measure the bolt elongation along the process, providing the translation into load value. Once the maximum pressure is reached, the nut locked and the tooling removed (step 4 in Figure 8), a full Hartman measurement is performed. It is also repeated several hours later to determine the effect of the relaxation.

5.3 Bolting Process

Bolting the PLATO EM Camera was done in two iterations, both depicted in Figure 9. The process followed the steps described above. In the first iteration (top panel of the figure), this corresponds to **1.** Hexapod at the nominal position (corresponding to the FPA nominal position); **2-5.** Gap measurement made, spacers installed and Hexapod elevated to ensure contact between the spacers and FPA-TOU interfaces; **6.** Tensioning tooling installed; **7-10.** Pre-tension increased in several steps; **11.** Maximum tension reached, nut locked and pressure released. The image acquisition is done after the load is released. The bolt tensioner is removed afterwards; **12** Measurement made the next day to check possible relaxation.

At this point, the detectors' position appeared out of the allowed range due to an unexpected level of embedding. A full Hartmann verification was performed to ensure it wasn't a local deviation, for instance linked to the non-flatness of the CCDs. It nevertheless confirmed that the FPA was 27 μm closer to the TOU than desired. Consequently, the integration had to be redone with thicker spacers. The bolts were removed and the next measure showed that the FPA returned to the nominal BIP position (step 13).

The bottom panel of Figure 9 shows the second and final iteration, with the following steps: **1.** Initial state (end of first iteration); **2.** the hexapod is lowered to allow for the spacers to be placed. The bolt tensioning tool is installed; **3-7.** The bolts are loaded gradually to the desired level, the nut is locked and the pressure is released; **8.** Bolt tensioning tool removed; **9.** Measurement made the next day, the position is within the desired range, alignment considered succesful. The final integration steps can be performed; **10.** After FPA MGSE removal (At this point the FPA is disconnected from the Hexapod); **11.** D+3: after thermal hardware installation; **12.** Final verification prior to MLI integration.

5.4 Bolting error budget

By doing several bolting iterations, some contributors to the bolting positioning error can be neglected in the final error budget for the bolting operation. For example, the embedding of the different mating surfaces or the possible movements due to manufacturing and assembly tolerances, while difficult to estimate theoretically are corrected by doing several iterations. On the EM specimen, their contribution was estimated by checking the FPA position with regards to the BiP position defined during the alignment. They were then compensated for by using thicker shims.

The final verification of the results on the EM camera proved that it was possible to predict the required spacer thickness with good accuracy based on the first bolting iteration, as well as to perform the operation with an excellent level of repeatability. With the current level of knowledge, two iterations are anticipated for the following specimen. The next cameras will also tell if the same levels of repeatability and accuracy can be achieved for all of them. This would imply that accurate prediction based on gap measurement (and other data gathered during the metrology study of the assembly) can be made to perform the bolting in only one iteration.

The remaining errors considered for the bolting error budget at this point are the manufacturing tolerance and the assembly of the spacers (8.0 μm) and the image position calculation error (3.0 μm), resulting in a final uncertainty on the bolting process of 8.5 μm.

Figure 9. Optical monitoring during the bolting. The grey curves show the position of the hexapod, i.e. the nominal position of the FPA. The orange curves indicates the location of the detector as traced by the size of the hartmann pattern measured at a constant position in the field of view. All measurements are relative to the initial, i.e. pre-bolting conditions. Every step on the x-axis corresponds to one image (e.g. after a change of the pressure exerted on the bolt tensioner). The first iteration is on top. The second one is below. The last step in the top panel and the first in the lower one are identical.

5.5 Optical Validation

A reference Hartmann measurement is performed at 40 positions in the field of view before and after the bolting process. A mosaic image of these 40 positions is presented in Figure 10. They were calculated to be in the center of cells covering identical surfaces on the sky while taking the small gaps between the CCDs into account. They consist in 4, 8, 12 and 16 positions at 3.1, 8.3, 12.4 and 16.33 degrees of elevation respectively. Close to the optical axis, an asymmetry in azimuth is visible between the 4 CCDs (section 2.2). The artefacts in the background, especially visible on the top-right, are due to cosmetic defects in the CCDs, which are not flight-grade.

The right panel of Figure 10 displays the comparison of this pre- vs post-integration optical verification. It shows that the measures are compatible with the absence of impact of the bolting process on the location of the focal plane within the measurement uncertainties.

The measurement performed after the camera integration is also used as a reference for a verification of the camera integrity throughout the rest of the AIV campaign: it is repeated before and after transport and before and after every cooldown sequence in the cryo-vacuum chambers. The camera underwent two cryo-vacuum test campaigns so far. The four associated reference measurements showed various relative displacements of the FPA in the focus direction, but no tilt. The largest defocus observed with respect to the outgoing reference measurement in CSL was $48\,\mu m$. The differences are nevertheless very well correlated with the temperature of the camera during the various measurements and are compatible with a trend of $dz/dT \sim 19\,\mu m/°C$, to be confirmed by additional measurements on this camera model as well as on the flight models.

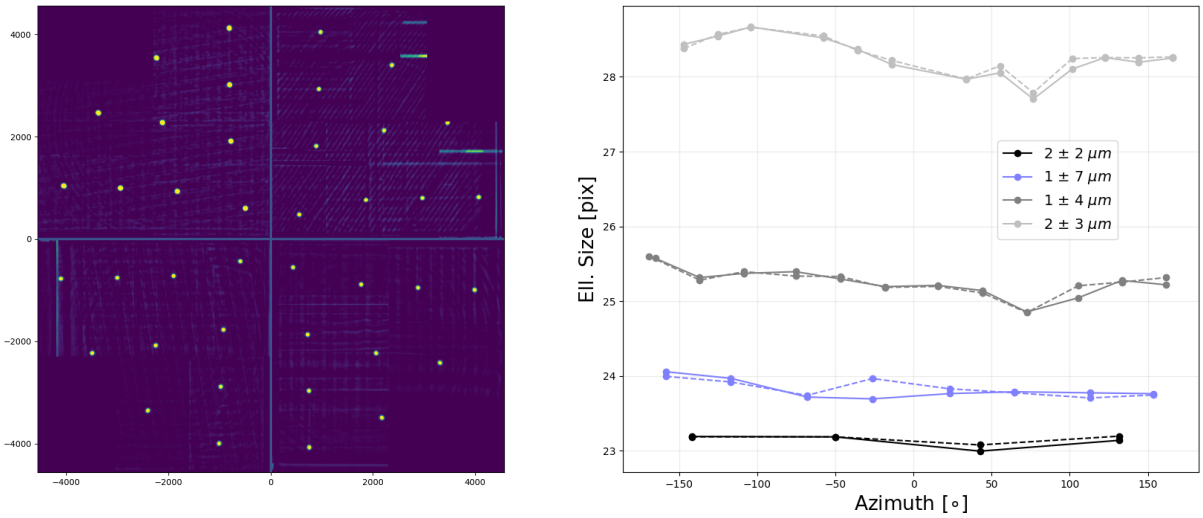

Figure 10. **Left**: Mosaic of the 40 positions visited in the field of view. **Right**: Post vs Pre-bolting measurements of the hartmann pattern, i.e. size of the hartmann pattern (Σ), as a function of the azimuth. The solid lines are pre-bolting, the dashed are post-bolting. The legend reports the differences. Elevation angles of 3.1, 8.3, 12.4 and 16.33 degrees are reported bottom-up. The enlargement of the hartmann pattern as a function of the elevation is due to the strong field curvature existing at ambient temperature.[15]

6. CONCLUSIONS

The Engineering Model camera of PLATO has been successfully produced, assembled and tested. The optical verifications of the metrology by analysis of a Hartmann pattern proved to be vital for this camera model. They were also demonstrated to be extremely sensitive and reproducible ($\sim 3\,\mu m$). The hartmann measurements performed at ambient before and after the cryo-vacuum test campaigns at SRON demonstrate a very good system stability despite the (expected) strong dependence of the defocus on the camera temperature, hence emphasizing the importance of common references for the temperature measurements performed during the optical characterization at TOU level prior to the assembly and at camera level during the assembly.

The AIV chain leading to the alignment and assembly of the camera and the associated metrology was validated by the optical performance of the camera, demonstrated under cryo-vacuum conditions at the SRON test-facility. The optical performance of the camera was found fully compliant with the requirements. Details on the corresponding tests and results can be found in Refs 19, 23, 13, 14.

ACKNOWLEDGMENTS

This work presents results from the European Space Agency (ESA) space mission PLATO. The PLATO payload, the PLATO Ground Segment and PLATO data processing are joint developments of ESA and the PLATO Mission Consortium (PMC). Funding for the PMC is provided at national levels, in particular by countries participating in the PLATO Multilateral Agreement (Austria, Belgium, Czech Republic, Denmark, France, Germany, Italy, Netherlands, Portugal, Spain, Sweden, Switzerland, Norway, and United Kingdom) and institutions from Brazil. Members of the PLATO Consortium can be found at https://platomission.com/. The ESA PLATO mission website is https://www.cosmos.esa.int/plato. The authors thank the Belgian Federal Science Policy Office (BELSPO) for the provision of financial support in the framework of the PRODEX Programme of the European Space Agency (ESA) under contract number PEA 4000137604. The Italian team at INAF acknowledges support from PLATO ASI-INAF agreement n. 2015-019-R.1-2018. Authors from INTA would like to thank to Agencia

Estatal de Investigación for the grant PID2019-107061GB-C62, which has been used as funding support for the activities described in this paper. We thank the teams working for PLATO for all their work.

REFERENCES

[1] Struve, O., "Proposal for a project of high-precision stellar radial velocity work," *The Observatory* **72**, 199–200 (Oct. 1952).

[2] Hale, A. and Doyle, L. R., "The Photometric Method of Extrasolar Planet Detection Revisited," *Astrophysics and Space Science* **212**, 335–348 (Feb. 1994).

[3] Christensen-Dalsgaard, J. and Aguirre, V. S., "Ages for Exoplanet Host Stars," in [*Handbook of Exoplanets*], Deeg, H. J. and Belmonte, J. A., eds., 184 (2018).

[4] Silva Aguirre, V., Davies, G. R., Basu, S., Christensen-Dalsgaard, J., Creevey, O., Metcalfe, T. S., Bedding, T. R., Casagrande, L., Handberg, R., Lund, M. N., Nissen, P. E., Chaplin, W. J., Huber, D., Serenelli, A. M., Stello, D., Van Eylen, V., Campante, T. L., Elsworth, Y., Gilliland, R. L., Hekker, S., Karoff, C., Kawaler, S. D., Kjeldsen, H., and Lundkvist, M. S., "Ages and fundamental properties of Kepler exoplanet host stars from asteroseismology," *MNRAS* **452**, 2127–2148 (Sept. 2015).

[5] Lebreton, Y. and Goupil, M. J., "Asteroseismology for "à la carte" stellar age-dating and weighing. Age and mass of the CoRoT exoplanet host HD 52265," *Astronomy and Astropysics* **569**, A21 (Sept. 2014).

[6] Rauer, H., Catala, C., Aerts, C., Appourchaux, T., Benz, W., Brandeker, A., Christensen-Dalsgaard, J., Deleuil, M., Gizon, L., Goupil, M. J., Güdel, M., Janot-Pacheco, E., Mas-Hesse, M., Pagano, I., Piotto, G., Pollacco, D., Santos, Ċ., Smith, A., Suárez, J. C., Szabó, R., Udry, S., Adibekyan, V., Alibert, Y., Almenara, J. M., Amaro-Seoane, P., Eiff, M. A.-v., Asplund, M., Antonello, E., Barnes, S., Baudin, F., Belkacem, K., Bergemann, M., Bihain, G., Birch, A. C., Bonfils, X., Boisse, I., Bonomo, A. S., Borsa, F., Brandão, I. M., Brocato, E., Brun, S., Burleigh, M., Burston, R., Cabrera, J., Cassisi, S., Chaplin, W., Charpinet, S., Chiappini, C., Church, R. P., Csizmadia, S., Cunha, M., Damasso, M., Davies, M. B., Deeg, H. J., Díaz, R. F., Dreizler, S., Dreyer, C., Eggenberger, P., Ehrenreich, D., Eigmüller, P., Erikson, A., Farmer, R., Feltzing, S., de Oliveira Fialho, F., Figueira, P., Forveille, T., Fridlund, M., García, R. A., Giommi, P., Giuffrida, G., Godolt, M., Gomes da Silva, J., Granzer, T., Grenfell, J. L., Grotsch-Noels, A., Günther, E., Haswell, C. A., Hatzes, A. P., Hébrard, G., Hekker, S., Helled, R., Heng, K., Jenkins, J. M., Johansen, A., Khodachenko, M. L., Kislyakova, K. G., Kley, W., Kolb, U., Krivova, N., Kupka, F., Lammer, H., Lanza, A. F., Lebreton, Y., Magrin, D., Marcos-Arenal, P., Marrese, P. M., Marques, J. P., Martins, J., Mathis, S., Mathur, S., Messina, S., Miglio, A., Montalban, J., Montalto, M., Monteiro, M. J. P. F. G., Moradi, H., Moravveji, E., Mordasini, C., Morel, T., Mortier, A., Nascimbeni, V., Nelson, R. P., Nielsen, M. B., Noack, L., Norton, A. J., Ofir, A., Oshagh, M., Ouazzani, R. M., Pápics, P., Parro, V. C., Petit, P., Plez, B., Poretti, E., Quirrenbach, A., Ragazzoni, R., Raimondo, G., Rainer, M., Reese, D. R., Redmer, R., Reffert, S., Rojas-Ayala, B., Roxburgh, I. W., Salmon, S., Santerne, A., Schneider, J., Schou, J., Schuh, S., Schunker, H., Silva-Valio, A., Silvotti, R., Skillen, I., Snellen, I., Sohl, F., Sousa, S. G., Sozzetti, A., Stello, D., Strassmeier, K. G., Švanda, M., Szabó, G. M., Tkachenko, A., Valencia, D., Van Grootel, V., Vauclair, S. D., Ventura, P., Wagner, F. W., Walton, N. A., Weingrill, J., Werner, S. C., Wheatley, P. J., and Zwintz, K., "The PLATO 2.0 mission," *Experimental Astronomy* **38**, 249–330 (Nov. 2014).

[7] Rauer, H., Pagano, I., Mas-Hesse, M., Aerts, C., Deleuil, M., Gizon, L., Goupil, M.-J., María Heras, A., Piotto, G., Pollacco, D., Ragazzoni, R., Ramsay, G., and Udry, S., "The PLATO mission: Overview and status," in [*European Planetary Science Congress*], EPSC2021–90 (Sept. 2021).

[8] Magrin, D., Ragazzoni, R., Bergomi, M., Biondi, F., Chinellato, S., Dima, M., Farinato, J., Greggio, D., Gullieuszik, M., Marafatto, L., Viotto, V., Munari, M., Pagano, I., Sicilia, D., Basso, S., Borsa, F., Ghigo, M., Spiga, D., Band y, T., Brändli, M., Benz, W., Bruno, G., De Roche, T., Piazza, D., Rieder, M., Brandeker, A., Klebor, M., Mogulsky, V., Schweitzer, M., Wieser, M., Erikson, A., and Rauer, H., "Manufacturing and alignment tolerance analysis through Montecarlo approach for PLATO," in [*Space Telescopes and Instrumentation 2016: Optical, Infrared, and Millimeter Wave*], MacEwen, H. A., Fazio, G. G., Lystrup, M., Batalha, N., Siegler, N., and Tong, E. C., eds., *Society of Photo-Optical Instrumentation Engineers (SPIE) Conference Series* **9904**, 99042Z (July 2016).

[9] Magrin, D., Ragazzoni, R., Rauer, H., Pagano, I., Nascimbeni, V., Piotto, G., Viotto, V., Piazza, D., Bandy, T., Basso, S., Benz, W., Bergomi, M., Biondi, F., Borsa, F., Börner, A., Brandeker, A., Brändli, M., Bruno, G., Cabrera, J., Calderone, F., Cessa, V., Chinellato, S., De Roche, T., Dima, M., Erikson, A., Farinato, J., Ghigo, M., Greggio, D., Klebor, M., Marafatto, L., Munari, M., Mogulsky, V., Pertenais, M., Peter, G., Portaluri, E., Rieder, M., Rockstein, S., Schweitzer, M., Sicilia, D., Umbriaco, G., Wieser, M., Heras, A. M., Marliani, F., Pirrotta, S., Salatti, M., Tommasi, E., Bardazzi, R., Battistelli, E., Brotini, M., Burresi, M., Capuano, E., Marinai, M., Novi, A., and Català, C., "PLATO: the ESA mission for exo-planets discovery," in [*Space Telescopes and Instrumentation 2018: Optical, Infrared, and Millimeter Wave*], Lystrup, M., MacEwen, H. A., Fazio, G. G., Batalha, N., Siegler, N., and Tong, E. C., eds., *Society of Photo-Optical Instrumentation Engineers (SPIE) Conference Series* **10698**, 106984X (July 2018).

[10] Moreno, J., Vielba, E., Manjón, A., Motos, A., Vázquez, E., Rodríguez, E., Saez, D., Sengl, M., Fernández, J., Campos, G., Muñoz, D., Mas, M., Balado, A., Ramos, G., Cerruti, C., Pajas, M., Catalán, I., Alcacera, M. A., Valverde, A., Pflueger, P., and Vera, I., "PLATO FPA. focal plane assembly of PLATO instrument," in [*International Conference on Space Optics; ICSO 2018*], *Society of Photo-Optical Instrumentation Engineers (SPIE) Conference Series* **11180**, 111803N (July 2019).

[11] Ramos, G., Valverde Guijarro, A. L., Rodrigo, M. T., Sierra, M. A., Gómez, L. J., Borreguero, E., Álvarez, L., Manjón, A., Balado, A., Barrado, D., and Mas, J. M., "Planetary transits and oscillation of stars (PLATO) focal plane assembly (FPA): prototype assembly and integration verification," in [*UV/Optical/IR Space Telescopes and Instruments: Innovative Technologies and Concepts IX*], Barto, A. A., Breckinridge, J. B., and Stahl, H. P., eds., **11115**, 49 – 59, International Society for Optics and Photonics, SPIE (2019).

[12] Laubier, D., Bodin, P., Pasquier, H., Fredon, S., Levacher, P., Vola, P., Buey, T., and Bernardi, P., "The PLATO camera," in [*Society of Photo-Optical Instrumentation Engineers (SPIE) Conference Series*], *Society of Photo-Optical Instrumentation Engineers (SPIE) Conference Series* **10564**, 1056405 (Nov. 2017).

[13] Vandenbussche, B. and et al., "The PLATO mission: camera thermal-vacuum performance verification and testing," in [*Society of Photo-Optical Instrumentation Engineers (SPIE) Conference Series*], *Society of Photo-Optical Instrumentation Engineers (SPIE) Conference Series* **12180**, 12180213 (Dec. 2022).

[14] Gorius, N. and et al., "Status of PLATO mission camera: recent progress on the camera engineering model and MAIV approach for the camera flight models," in [*Society of Photo-Optical Instrumentation Engineers (SPIE) Conference Series*], *Society of Photo-Optical Instrumentation Engineers (SPIE) Conference Series* **12180**, 1218046 (Dec. 2022).

[15] Royer, P., Clermont, L., Pertenais, M., Baeke, A., Huygen, R., De Ridder, J., Regibo, S., Dami, M., Vandenbussche, B., Belen Balado Margeli, A., Farinato, J., Greggio, D., Levillain, Y., Magrin, D., Marafatto, L., Pajas, M., Ramos Zapata, G., Valverde Guijarro, A. L., and Viotto, V., "On the optical alignment of the PLATO cameras," in [*Society of Photo-Optical Instrumentation Engineers (SPIE) Conference Series*], *Society of Photo-Optical Instrumentation Engineers (SPIE) Conference Series* **11443**, 114434Q (Dec. 2020).

[16] Pagliazzi, M. and et al., "Precise localization of the best image plane of PLATO telescope optical units," in [*Society of Photo-Optical Instrumentation Engineers (SPIE) Conference Series*], *Society of Photo-Optical Instrumentation Engineers (SPIE) Conference Series* **12180**, 1218216 (Dec. 2022).

[17] Abreu, M., Castro Alves, D., Cabral, A., Coelho, J. M. P., Santos, P., Clermont, L., Baeke, A., and Vandenbussche, B., "A white light collimator for Plato camera integration support," in [*Society of Photo-Optical Instrumentation Engineers (SPIE) Conference Series*], *Society of Photo-Optical Instrumentation Engineers (SPIE) Conference Series* **11443**, 114434T (Dec. 2020).

[18] Regibo, S., Huygen, R., Royer, P., Vandenbussche, B., and Ruiz de Galarreta Fanjul, C., "Design of the electrical ground support equipment for the PLATO camera AIV," in [*Society of Photo-Optical Instrumentation Engineers (SPIE) Conference Series*], *Society of Photo-Optical Instrumentation Engineers (SPIE) Conference Series* **11443**, 1144351 (Dec. 2020).

[19] Borsa, F., Gorius, N., Cottinelli, A., and et al., "PLATO EM cryogenic vacuum test campaign results," in [*Society of Photo-Optical Instrumentation Engineers (SPIE) Conference Series*], *Society of Photo-Optical Instrumentation Engineers (SPIE) Conference Series* **12180**, 1218050 (Dec. 2022).

[20] Clermont, L., Jacobs, J., Blain, P., Abreu, M., Vandenbussche, B., Royer, P., Huygen, R., Halain, J., and Baeke, A., "Automatized alignment of the focal plane assemblies on the PLATO cameras," in [*Society of*

Photo-Optical Instrumentation Engineers (SPIE) Conference Series], *Society of Photo-Optical Instrumentation Engineers (SPIE) Conference Series* **10698**, 10698L (Aug. 2018).

[21] Yen, J.-C., Chang, F.-J., and Chang, S., "A new criterion for automatic multilevel thresholding," *IEEE Transactions on Image Processing* **4**(3), 370–378 (1995).

[22] Cottinelli, A., Vassallo, D., Farinato, J., Magrin, D., Biondi, F., Ragazzoni, R., Pagano, I., and et al., "Hartmann data analysis for PLATO TOU EM," in [*Society of Photo-Optical Instrumentation Engineers (SPIE) Conference Series*], *Society of Photo-Optical Instrumentation Engineers (SPIE) Conference Series* **12180**, 12180212 (Dec. 2022).

[23] Pertenaïs, M., Ammler-von Eiff, M., Burresi, M., Cabrera, J., J., F., Gorius, N., T., K., Magrin, D., Munari, M., Regibo, S., Royer, P., Vandenbussche, B., and van Kempen, T., "PLATO Camera Ghosts: simulations and measurements on the Engineering Model (EM)," in [*Society of Photo-Optical Instrumentation Engineers (SPIE) Conference Series*], *Society of Photo-Optical Instrumentation Engineers (SPIE) Conference Series* **12180**, 12180215 (Dec. 2022).